Microstructure and Mechanical Properties of Hypoeutectic Al-6Ce-3Ni-0.7Fe (wt.%) Alloy

Tiffany Wu[1], A. Plotkowski[2], A. Shyam[2], David C. Dunand[1,*]

Email: TiffanyWu2024@u.northwestern.edu, plotkowskiaj@ornl.gov, shyama@ornl.gov, dunand@northwestern.edu

[1] Department of Materials Science & Engineering, Northwestern University, Evanston, IL 60208-3108, USA

[2] Materials Science & Technology Division, Oak Ridge National Laboratory, Oak Ridge, TN, USA

* Corresponding author

Abstract

A hypoeutectic, Fe-modified Al-Ce-Ni alloy (Al-6Ce-3Ni-0.7Fe, wt.%) is studied in terms of microstructure, thermal stability, ambient temperature strengthening, and creep resistance. Laser-remelting on cast alloy is done to investigate the high undercooling effects. The as-cast microstructure consists of primary Al dendrites and interdendritic binary eutectic regions (Al-$Al_{11}Ce_3$ and/or Al-$Al_9(Fe,Ni)_2$), with micron/submicron lamellar spacing, depending on the location along the height of the ingot. The cast alloy exhibits excellent coarsening resistance at 400 °C, with mostly unchanged microstructure and microhardness after 6 weeks of aging, indicating good thermal stability of $Al_{11}Ce_3$ and $Al_9(Fe,Ni)_2$. Orowan strengthening and load transfer are identified as strengthening mechanisms at ambient and elevated temperature. A high volume fraction of the intermetallic phases (providing load transfer) and relatively coarse eutectic spacing (for modest Orowan strengthening) result in a moderate as-cast microhardness of 566±32 MPa. Creep resistance at 300 and 350 ºC is similar to a binary Al-12.5Ce eutectic alloy (with twice the Ce content) because of two countering effects: Al-6Ce-3Ni-0.7Fe shows a higher volume fraction of strengthening intermetallic phases, but it also exhibits a large fraction of primary Al dendrites which weaken the alloy. By contrast, the laser-remelted alloy has a fully eutectic microstructure without primary aluminum dendrites achieved by high undercooling, with a refined network of eutectic phase that doubles the microhardness as compared to the cast alloy. Whereas coarsening is faster due to the shorter diffusion distances between the eutectic phases, hardness remains ~30% higher than the as-cast alloy after ~6 weeks aging at 400 °C.

Introduction

Most commercial aluminum alloys experience significant strength loss above ~250 °C due to coarsening and/or dissolution of strengthening precipitates formed upon aging [1]. By contrast, alloys strengthened with $L1_2$-$Al_3(Sc,Zr)$ nanoprecipitates exhibit, up to ~300 °C, good coarsening resistance (from the low diffusivity of Sc and Zr in Al) and high creep resistance from a high number density of coherent precipitates which impede dislocation climb [2–7]. Also, near-eutectic Al-alloys show superior creep resistance, owing to the high volume fraction of intermetallic phases formed upon solidification which strengthen the matrix via load transfer to the strong intermetallic phases [8,9]. Additional strengthening can be accomplished by inhibiting dislocation motion in the matrix of eutectic alloys with very fine eutectic phase spacing, as achieved by rapid solidification, in particular *via* melt-based additive manufacturing (AM) methods. Among various Al-based eutectic systems (e.g., Al-Cu [10–12], Al-Si [13–15], Al-Mg-Si [16], Al-Ni [9,17–20], Al-Ce [8,21–24]), the Al-$Al_{11}Ce_3$ eutectic stands out because of its outstanding coarsening resistance, owing to the very low solubility and diffusivity of Ce in Al [25]. Cast, near-eutectic Al-Ce(-Mg) alloys show little change in microhardness and microstructure after long-term exposure at 400 °C [8,26], and the interconnected, plate-like $Al_{11}Ce_3$ eutectic phase (often labelled as "Chinese script") exhibits much less coarsening than Al_3Ni rods in Al-Ni eutectic alloys [27] or Si platelets in Al-Si eutectic alloys [14]. The creep resistance of near-eutectic Al-12.5Ce (all composition are hereafter given in wt.%) is higher than many of the $L1_2$-strengthened Al-Sc-Zr alloys at 300°C [8], but slightly lower than that of the near-eutectic Al-6.4Ni alloy [9]. The good creep resistance of Al-12.5Ce originates from load partitioning from the pure Al matrix to the $Al_{11}Ce_3$ intermetallic phase [22,26], which, as a pure phase, has microhardness (~4 GPa) and creep resistance much higher than pure Al [28].

With Al-Ce eutectic as the base microstructure, additional strengthening can be achieved by nano-precipitates (Al-Ce-Sc [21]), solid solution (Al-Ce-Mg [26]), and/or other eutectic phases (Al-Ce-Ni [27]). Cast, near-eutectic Al-10Ce-5Ni displays fine, coupled $Al_{11}Ce_3$-Al_3Ni intermetallic phases in a nearly-pure Al matrix, which improve both hardness and creep resistance *via* Orowan strengthening and load partitioning [27]. Cast, near-eutectic Al-10Ce-5Ni [27] and AM Al-10.5Ce-3.1Ni-1.2Mn [29] show excellent creep properties. Here, to improve on existing Al-Ce-Ni alloys, we replace some Ni with Fe, which is less costly than Ni. In addition, compared to Ni, Fe has significantly lower solubility (~0.02 vs. 0.06 at.%) and slightly lower diffusivity (1.3×10^{-17} vs. 2.3×10^{-17} m^2/s) in Al at 400 °C [30,31], which should provide enhanced coarsening resistance as compared to Al_3Ni [9]. For Al-Ni-Fe ternary system, a eutectic reaction takes place at a composition of Al-6.7Ni-0.2Fe, forming Al, Al_3Ni, and $Al_9(Fe,Ni)_2$ at 638°C [32]. While primary Al_3Fe can form at slow cooling rates [33], many Al-Fe-Ni alloys exhibit the Al-$Al_9(Fe,Ni)_2$ eutectic phase [33–37], which has good coarsening resistance at elevated temperature ($\geq$ 300 °C) [34,37].

In this study, we investigate the microstructure, thermal stability, and strengthening of a hypo-eutectic, quaternary Al-6Ce-3Ni-0.7Fe alloy, where Fe partially replaces Ni and where Ce is reduced as compared to the previously-studied Al-10Ce-5Ni [27] near-eutectic alloy. Coarsening of the eutectic phases during isothermal aging is studied by following the change of Vickers microhardness in relation to the evolving microstructures. Creep properties of the as-cast alloy are measured to assess strengthening at elevated temperatures. Lastly, laser-remelting of the cast alloy is performed to achieve refined microstructures, through processing directly applicable to laser powder bed fusion (LPBF).

Experimental Procedures

A hypo-eutectic quaternary alloy with Al-6Ce-3Ni-0.7Fe (wt.%) nominal composition was made by arc-melting atomized powders. The arc-melted ingot was then remelted in a graphite crucible at 800 °C in air, and the melt was stirred manually at regular intervals over 30 min. The furnace temperature was raised to, and held at, 850 °C for 5 min before pouring the melt into a graphite mold, which was preheated at 200 °C and placed on an ice-cooled copper plate just before pouring to promote directional solidification (cooling rate ~15 K/s) of the alloy. Three cylindrical ingots (~65 mm in length, ~15 mm in diameter) were extracted from the mold. The chemical composition was determined to be close to the nominal composition, using slices from top and bottom regions of the ingot, as summarized in Table.1. Measurements were performed via inductivity-coupled argon plasma optical emission spectroscopy (ICP-OES) at Dirats Laboratories (Westfield, MA).

For laser-remelting experiments, slices (~15 mm in diameter, ~5 mm in thickness) were cut from the cylindrical ingot and ground with 600 grit paper. Four 3 × 3 mm regions were remelted in a LPBF instrument (LASERTEC 12 SLM, from DMG Mori) with laser beam size of 55 μm at 400 W power at 800 mm/s scanning speed under Ar atmosphere. Each sample was cut perpendicularly to the laser travel direction to reveal cross-section of the melt pools and was polished for metallographic examination and microhardness measurements.

For cast samples, 5 mm thick slices from the top and bottom regions of the ingot were used for isothermal aging at 400 °C for up to 1050 h (~6 weeks), terminated by water quenching. Isothermal overaging was performed at 590 °C for 24 h. Laser-remelted samples were aged under the same condition, except for overaging. Vickers microhardness was measured on both slices, polished to 8 μm surface finish, under a 200 g load for 5 s with at least twelve indents per slice, using a Wilson VH3100 automated microhardness tester (Buehler).

To achieve deep etching, polished samples were immersed in a concentrated sodium hydroxide solution (10 g of NaOH pellets dissolved in 40 ml of distilled water) and rinsed under distilled water repeatedly, until the Al matrix was partially dissolved. A scanning electron microscope (SEM) JEOL JSM-7900FLV, equipped with energy dispersive spectroscopy (EDS), was used for microstructure characterization. X-ray diffraction was performed using a PANaltyical X'Pert MPD Pro instrument, with a Cu source configured with a 1/2° divergence slits. Data were measured for 2θ angles between 25 and 120° with a 0.0167° step size using an X'Celerator detector.

Compression creep testing was performed at 300 and 350 °C on as-cast cylindrical samples (7 mm diameter and 15 mm height), extracted from cast ingots *via* electrical discharge machining. Creep samples, held between two BN-coated WC-Co plates in a compression fixture, were placed in a three-zone furnace (with temperature fluctuations of ±2°C) with a thermocouple placed in contact with the specimen. Compressive stress was applied *via* a lever arm and dead weights, and deformation was measured by a linear variable displacement transducer using an extensometer connected to the compression cage. Tests were carried out at increasing stress levels and terminated once the sample had accumulated a strain of ~10%. For each level, the load was maintained until a steady-state strain rate was clearly measurable, as determined from strain vs. time plots.

Table 1. Alloy composition (wt.%) for top and bottom regions of cast ingot.

	Al	Ce	Ni	Fe	Si
Nominal	Bal.	6.0	3.0	0.7	<0.1
Top	Bal.	5.94	3.04	0.68	0.094
Bottom	Bal.	6.00	3.01	0.61	0.094

Experimental Results

i. As-cast microstructure

Figure 1 shows the X-ray diffraction spectrum of the as-cast Al-6Ce-3Ni-0.7Fe (wt.%) hypoeutectic alloy taken from top part of the ingot, indicating that the three major phases are Al, $Al_{11}Ce_3$, and $Al_9(Fe,Ni)_2$. The same phases were found in the diffraction spectrum for the bottom of the ingot (Fig. S1). However, different microstructures are found across the ingot: Figures 21(a,c,e) show the "coarse microstructure" and Figs. 2 (b,d,f) show the "fine microstructure" that are dominant at top and bottom of the ingot respectively. The microstructure across the ingot is a mixture of coarse and fine microstructures, which probably reflect varying cooling rates across the ingot rather than compositional variation (Table 1). In Fig.2 (c), the coarse microstructure consist of long Al dendrites (>10 μm) containing $Al_9(Fe,Ni)_2$ plates (as shown in the red dash box), and interdendritic regions consisting of alternating, Al-$Al_{11}Ce_3$ /Al-$Al_9(Fe,Ni)_2$ binary eutectic lamellar phase with spacing ~700 nm (indicated with yellow dash box). Figure 2 (e) shows the deep-etched microstructure, with the Al matrix partially dissolved, revealing the morphology of the $Al_{11}Ce_3$ and $Al_9(Fe,Ni)_2$ phases, which can be described as lamellar-interconnected, i.e., "Chinese script" and lamellae respectively. For the fine microstructure (Figs. 2 (b,d,f)), Al dendrites are much finer (<10 μm) and disconnected, and binary Al-$Al_{11}Ce_3$ eutectic (eutectic spacing ~200 nm), together with micron-sized $Al_9(Fe,Ni)_2$ plates, form between the dendrites. In Fig.2 (e,f), for both coarse and fine microstructures, $Al_{11}Ce_3$ has a "Chinese script" morphology similar to that reported in cast near-eutectic Al-12.5Ce [8]. Most of the eutectic volume consists of binary eutectic regions (Al+$Al_{11}Ce_3$ and/or Al+$Al_9(Fe,Ni)_2$), with rare occurrences of ternary eutectic regions (Al+$Al_{11}Ce_3$+$Al_9(Fe,Ni)_2$) microstructure (Fig. S2). Also, Al_3Ni eutectics (Fig. S3) are occasionally observed throughout the sample but their low volume fraction is expected to limit their effect on bulk mechanical properties.

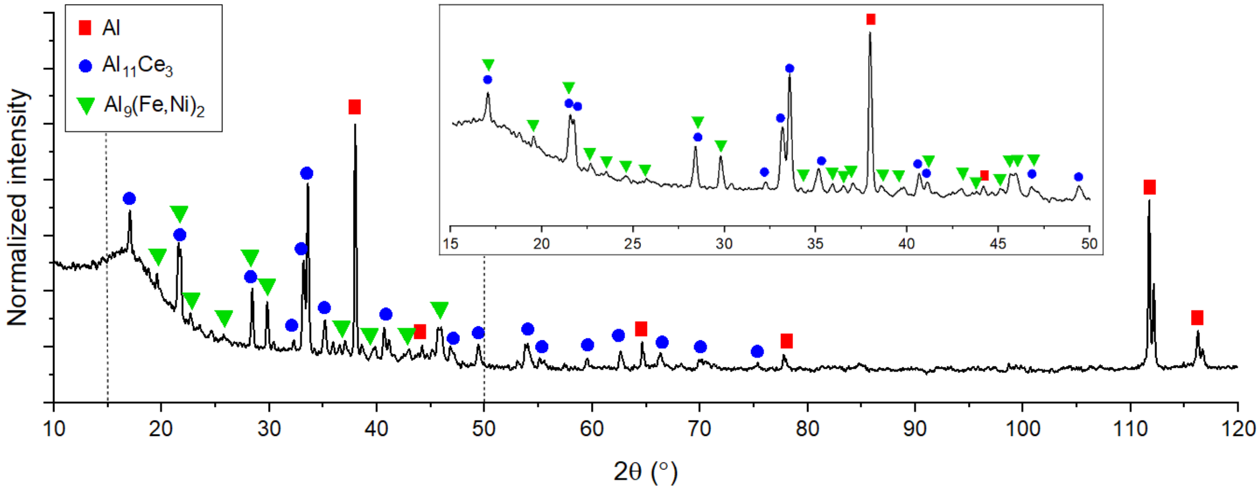

Fig. 1. X-ray diffraction pattern for as-cast Al-6Ce-3Ni-0.7Fe alloy. Insert is a magnified view at lower angles (range between dash lines) showing major peaks of the $Al_9(Fe,Ni)_2$ phase.

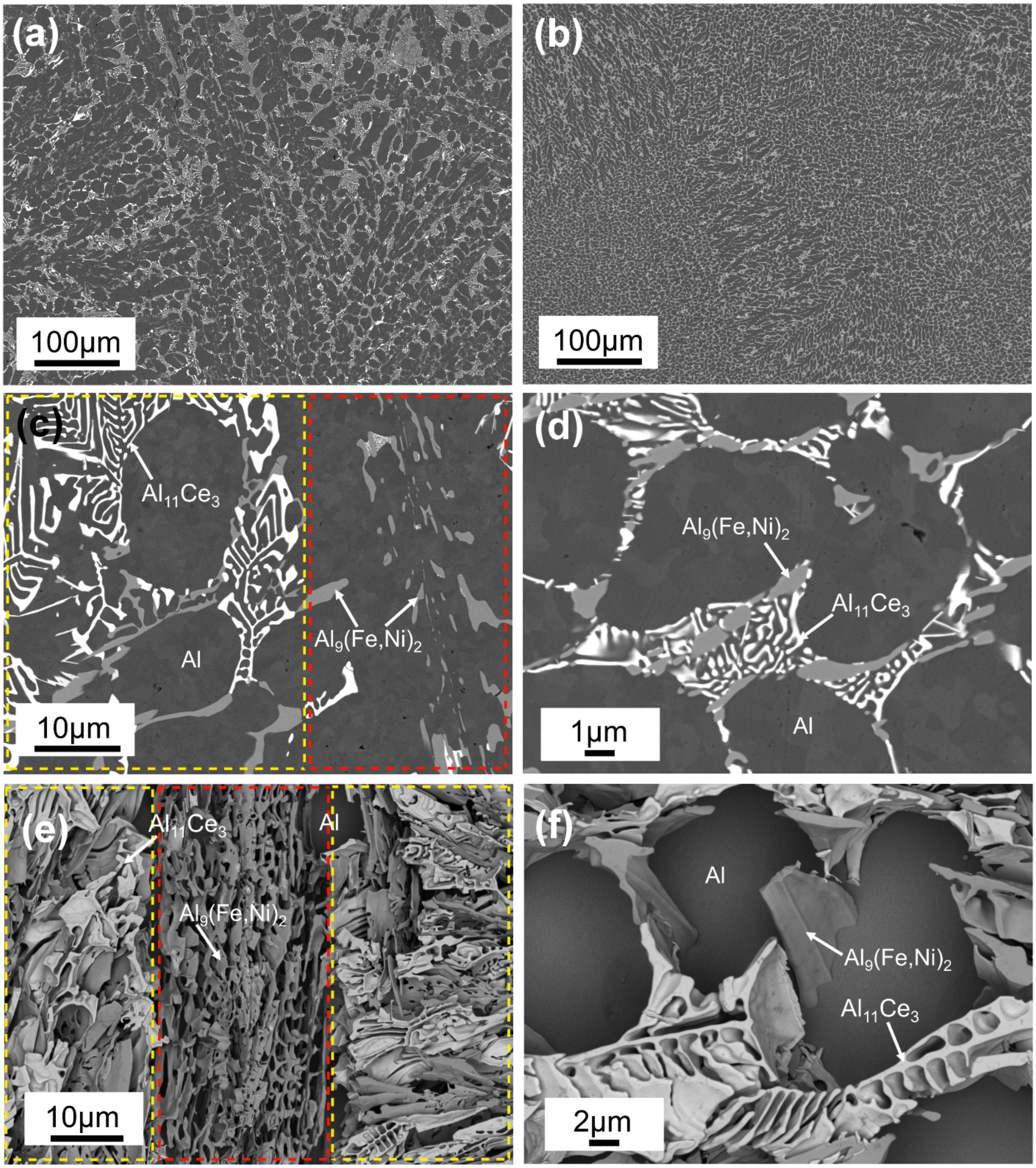

Fig. 2. BSE-SEM micrographs of as-cast Al-6Ce-3Ni-0.7Fe from (a,c,e) top and (b,d,f) bottom of ingot, showing "coarse" and "fine" microstructures, respectively. (e-f) deep-etched views of microstructure shown in (c-d) respectively. Black, grey, and white phases are identified as Al-matrix, $Al_9(Fe,Ni)_2$, and $Al_{11}Ce_3$ phases respectively. In (c,e), the red dash box indicates a region with Al-dendrites + $Al_9(Fe,Ni)_2$, sandwiched between two yellow dash boxes indicating volumes with alternating Al-$Al_{11}Ce_3$ and Al-$Al_9(Fe,Ni)_2$ binary eutectics.

ii. Isothermal aging

Figure 3 shows the evolution of Vickers microhardness of cast and laser-remelted (microstructure discussed in Section v) Al-6Ce-3Ni-0.7Fe during isothermal aging at 400 °C. The cast alloy shows a near-constant microhardness up to 1050 h (~6 weeks) of aging, unlike the laser-remelted hardness whose unaged hardness (which is twice the cast value) gradually decreases with aging time, dropping by ~30% below the as-remelted microhardness after ~6 weeks. For the cast alloy, the aged microstructure (Fig. 4) remains nearly unchanged as compared to the as-cast state (Fig.2), except for the coarsening of Al_3Ni particles, as indicated in yellow circles in Fig. 4. As shown at higher magnification in Fig. 4 (b), while the eutectic $Al_9(Fe,Ni)_2$ and $Al_{11}Ce_3$ phases remain mostly unchanged, the coarsened Al_3Ni particles partially engulf the other two intermetallic phases, as also observed in cast Al-10Ce-5Ni [27].

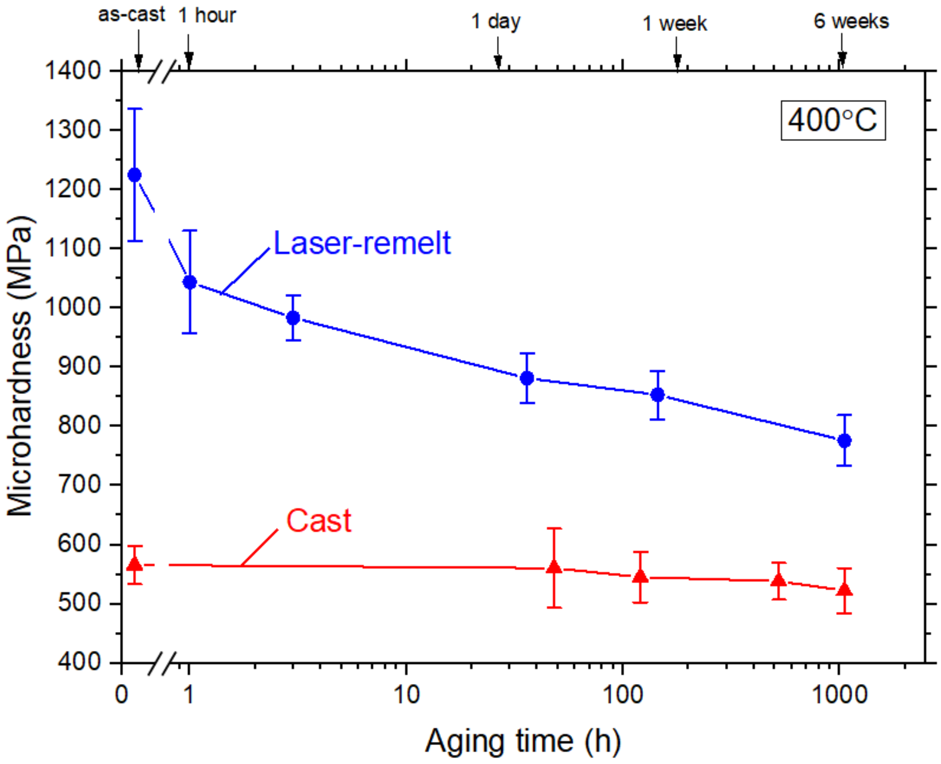

Fig.3. Evolution of Vickers microhardness for cast and laser-remelted Al-6Ce-3Ni-0.7Fe upon aging at 400 °C.

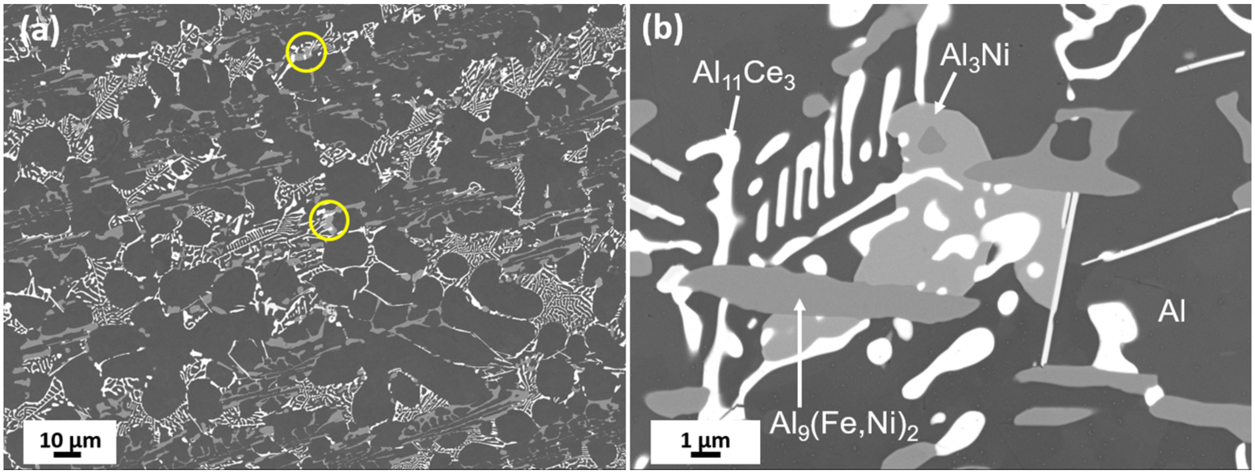

Fig. 4. BSE-SEM micrographs of aged (400 °C, 1050h) Al-6Ce-3Ni-0.7Fe, showing phases with different contrast (from darkest to brightest) identified as: Al-matrix, $Al_9(Fe,Ni)_2$, Al_3Ni, and $Al_{11}Ce_3$. (a) low-magnification micrograph of the coarsened microstructure, with yellow circles showing infrequent regions with coarsened Al_3Ni and (b) high-magnification micrograph of a yellow circle, showing a coarsened Al_3Ni particle partially engulfing $Al_9(Fe,Ni)_2$ and $Al_{11}Ce_3$ eutectics.

iii. Overaged microstructure

Overaging at 590 °C for 24 h was performed to hasten extreme coarsening on the microstructure. Similar diffraction pattern as as-cast sample (Fig. S1) indicates no new phases formed after overaging. The cast alloy undergoes a relatively mild 16% drop of microhardness from 566±32 (as-cast) to 479±26 MPa (overaged). Figure 5a shows the overaged microstructure where intermetallic phases are fragmented and coarsened into irregular-shaped precipitates ($Al_{11}Ce_3$) and plate-like precipitates ($Al_9(Fe,Ni)_2$) as shown in the deep-etched microstructure (Fig. 5b). Silicon+cerium+nickel-rich platelets, originating from the relatively high level of Si-impurity (Table 1) and found in the as-cast state, have becomes coarser after overaging; nevertheless, their volume fraction is quite low (~3 vol.%) to significantly impact macroscopic mechanical properties. Fig. 6 shows EDS mapping on a magnified view of the overaged microstructure with all phases present labelled: Al-matrix, $Al_9(Fe,Ni)_2$, Al_3Ni, and $Al_{11}Ce_3$, and Si+Ce+Ni-rich phases (indicated by yellow arrows).

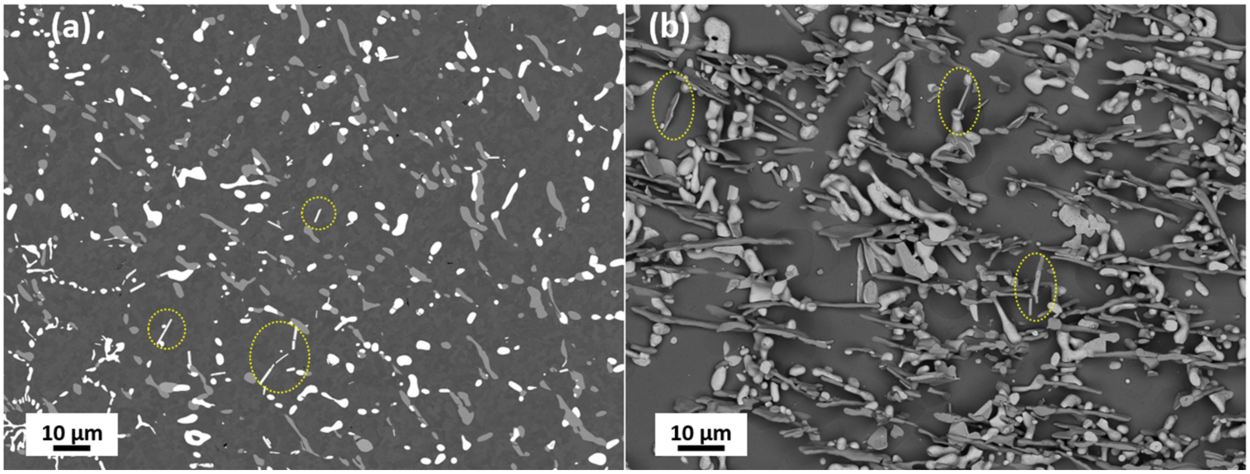

Fig. 5. BSE-SEM micrographs of Al-6Ce-3Ni-0.7Fe overaged at 590 °C for 24 h: (a) polished cross-section and (b) deep-etched microstructure. Yellow dotted circles are Si+Ce+Ni-rich phases (from Si impurities).

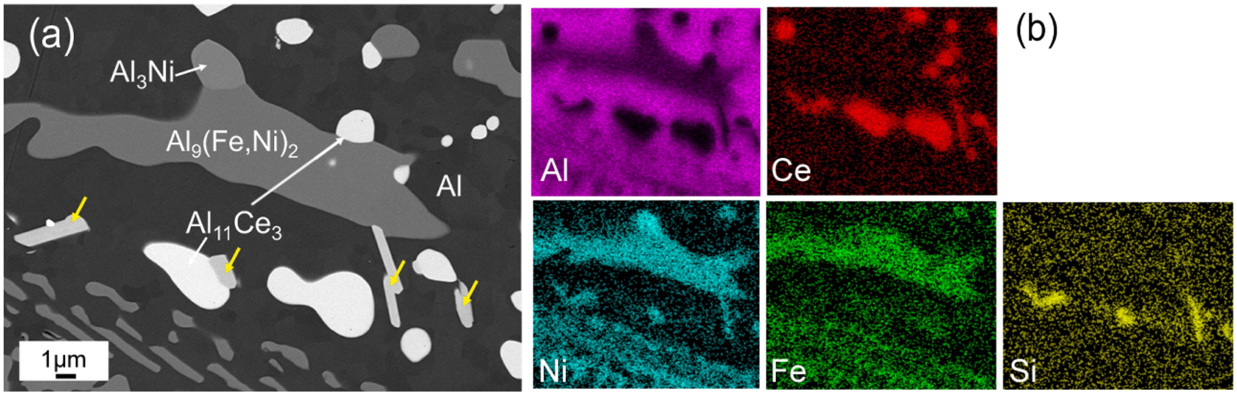

Fig. 6. (a) BSE-SEM micrograph of Al-6Ce-3Ni-0.7Fe overaged at 590 °C for 24 h and (b) corresponding EDS maps, showing phases at different contrast (from darkest to brightest): Al-matrix, $Al_9(Fe,Ni)_2$, Al_3Ni, Si+Ce+Ni-rich phase (pointed with yellow arrows) and $Al_{11}Ce_3$.

iv. Creep Properties

The compression creep behavior of cast Al-6Ce-3Ni-0.7Fe, tested at 300 and 350 °C, is shown in a double-logarithmic plots of minimum creep strain rate $\dot{\varepsilon}$ vs. applied stress σ in Fig. 7. Data are fitted with a power-law equation [38]:

$$\dot{\varepsilon} = A\sigma^{n_{app}} \exp\left(-\frac{Q_{app}}{RT}\right) \tag{1}$$

where A is a constant, n_{app} is the apparent stress exponent, Q_{app} is the apparent activation energy, R is the ideal gas constant, and T is the absolute temperature. The slight increase in slope (apparent stress exponent) from low to high stress level might indicate a transition from diffusional to dislocation creep. For the dislocation creep regime, the apparent stress exponents are much higher than that of pure Al (n=4.4), indicating the presence of a threshold stress σ_{th} that inhibits dislocation creep. Therefore, Equation (1) can be rewritten as follow [38]:

$$\dot{\varepsilon} = A'(\sigma - \sigma_{th})^n \exp\left(-\frac{Q}{RT}\right) \qquad (2)$$

where A' is a constant, n=4.4 is the stress exponent of the Al matrix, and Q is the creep activation energy for the matrix. The threshold stress σ_{th} is determined by fitting the linear part of a $\dot{\varepsilon}^{1/4.4}$ vs. σ linear plot at higher strain rate region and extrapolating to $\dot{\varepsilon} = 0$. Since data are insufficient in the diffusional creep regime, only calculated σ_{th} and n_{app} for dislocation creep are reported in Fig. 7. As shown in Fig. 7, as-cast Al-6Ce-3Ni-0.7Fe -a,b (from top and bottom part of the ingot respectively) have comparable creep resistance at 300 °C, with Al-6Ce-3Ni-0.7Fe-a (with majority of coarse microstructure) being slightly less creep resistant. Specimen c, tested at 350 °C, was taken from the middle part of the ingot, so its creep response is assumed to be an average between those of the coarse and fine microstructures (Fig. 2). Creep resistance at 300 °C is much higher than at 350 °C as expected, and the apparent stress exponents are the same for all three samples (12).

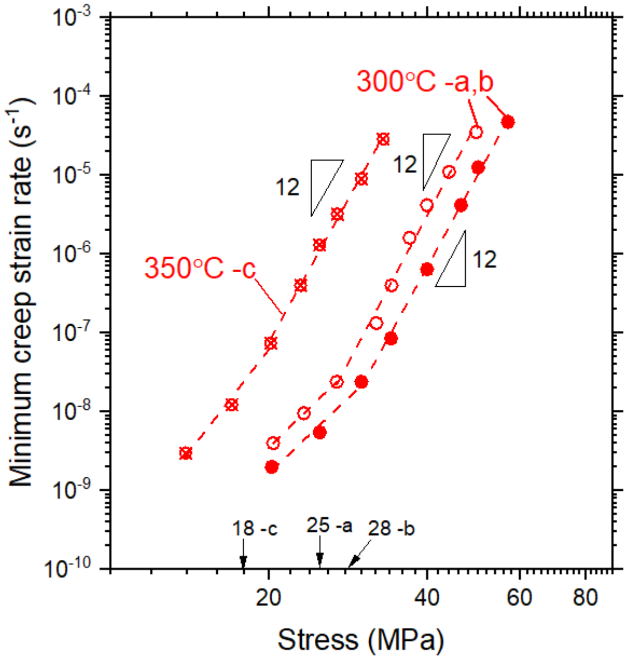

Fig. 7. Double-logarithmic plot of minimum creep strain rate vs. compressive stress for as-cast Al-6Ce-3Ni-0.7Fe at 300 and 350 ˚C, with best-fit lines drawn using Eq. (1). Threshold stresses determined from Eq. (2) are marked with arrows on x-axis. Samples a, b, and c are from top, bottom, and middle part of the ingot respectively.

v. Laser-remelting

Figure 8 shows the microstructure of cross-sections of the laser-remelted Al-6Ce-3Ni-0.7Fe alloy, perpendicular to the scanning direction. The laser-remelted region (with yellow dashed line highlighting several melt-pool boundaries) and the underlying cast region are visible in Fig. 8 (a). With high scanning power (400 W) and moderate scanning speed (800 mm/s), the high volumetric energy density results in deep (~350 μm) and narrow melt pools containing occasional keyhole pores, as indicated with a white arrow. A representative melt-pool boundary is imaged at higher magnification in Fig. 8 (b), showing that the eutectic structure is coarser at the boundary and finer within the melt pool. Eutectic scales are slightly different across the melt pool with coarser/finer eutectics from at the middle/ bottom of the melt pool in Figs. 8 (c)/(d) respectively. As compared to the cast microstructure with a eutectic spacing of ~200-700 nm, the laser-remelted regions show a much finer eutectic network (~50-70 nm). Exact phase and morphology identification will be studied in later work, as the goal of the present study is to assess how the refined microstructure improves mechanical properties.

Figure 9 shows the microstructure evolution at 400°C, from the as-remelted, unaged state to a long-term aging of 1050 h. Coarsening occurs more rapidly along grain boundaries (highlighted with yellow dash lines) than within the grains, resulting in coarse, irregular-shaped Ni/Fe- and/or Ce-rich precipitates (grey/white, marked with yellow arrows) surrounded by eutectic-free zones. In addition, the eutectic networks within the melt pools fragment, spheroidize, and coarsen as aging time increases. Grey elongated precipitates (highlighted with white arrows), tentatively identified as a Ni/Fe-rich phase, forms and coarsens during aging, and these precipitates appear to have well defined orientations with the grain, consistent with the existence of a crystallographic orientation relationship. Similar Ni/Fe-rich phase has been found in unpublished work [39] on AM of Al-6Ce-3Ni-0.7Fe upon aging using STEM EDS mapping. Coarsening of the microstructure clearly proceeds with aging time as shown in Fig. 9, which is consistent with the decreasing microhardness during aging reported in Fig. 3.

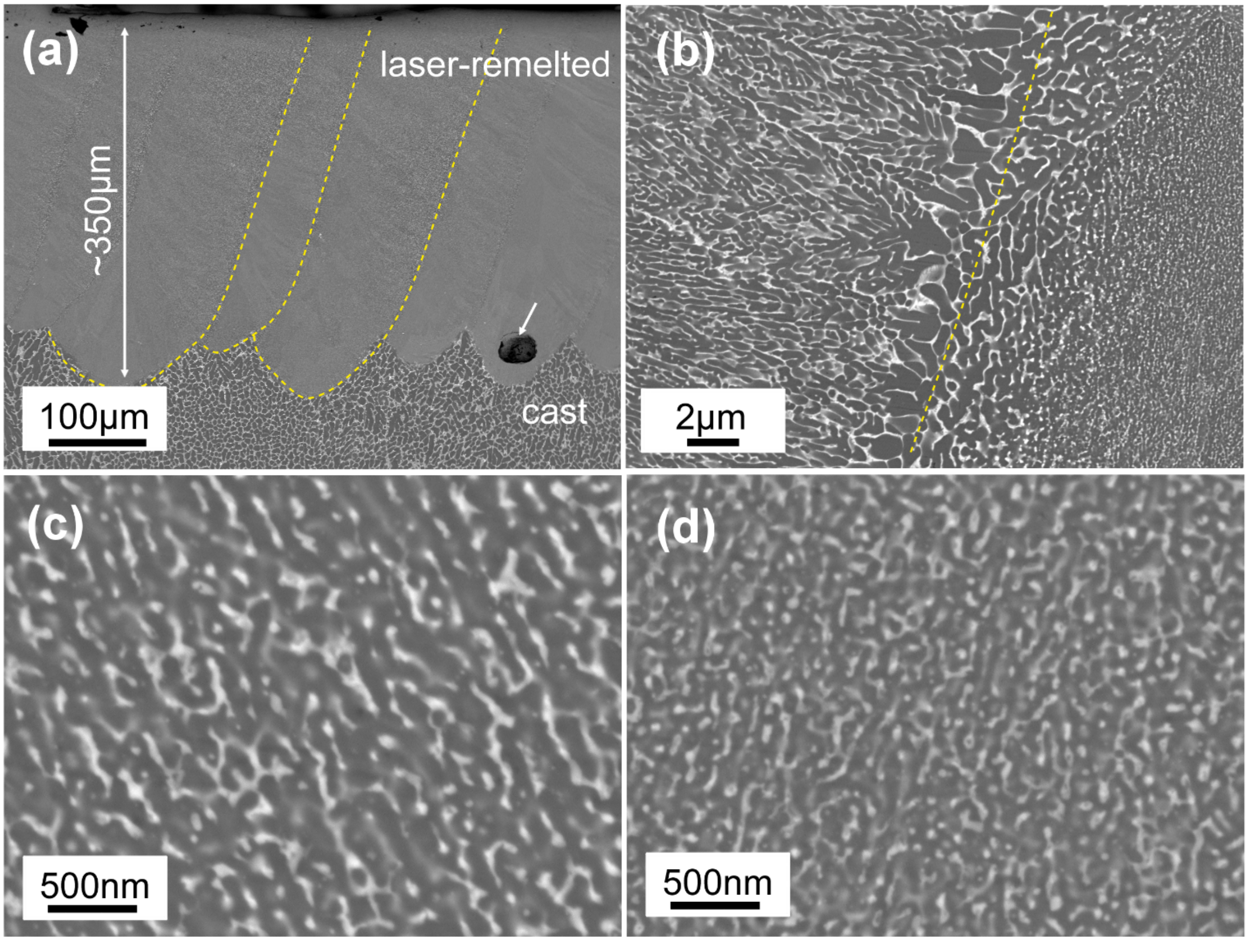

Fig. 8. BSE-SEM micrographs of laser-remelted cast Al-6Ce-3Ni-0.7Fe (perpendicular to scanning direction). (a) Overview of laser-remelted and underlying cast microstructure, with examples of melt-pool boundary highlighted with yellow dash-lines. Arrow points at a keyhole pore. Remelted surface is at top. (b) High magnification view of vertical melt pool boundary, where phases are coarser than within the melt pool. (c,d) High magnification view of eutectic microstructure from middle (c) and bottom (d) of the melt pool.

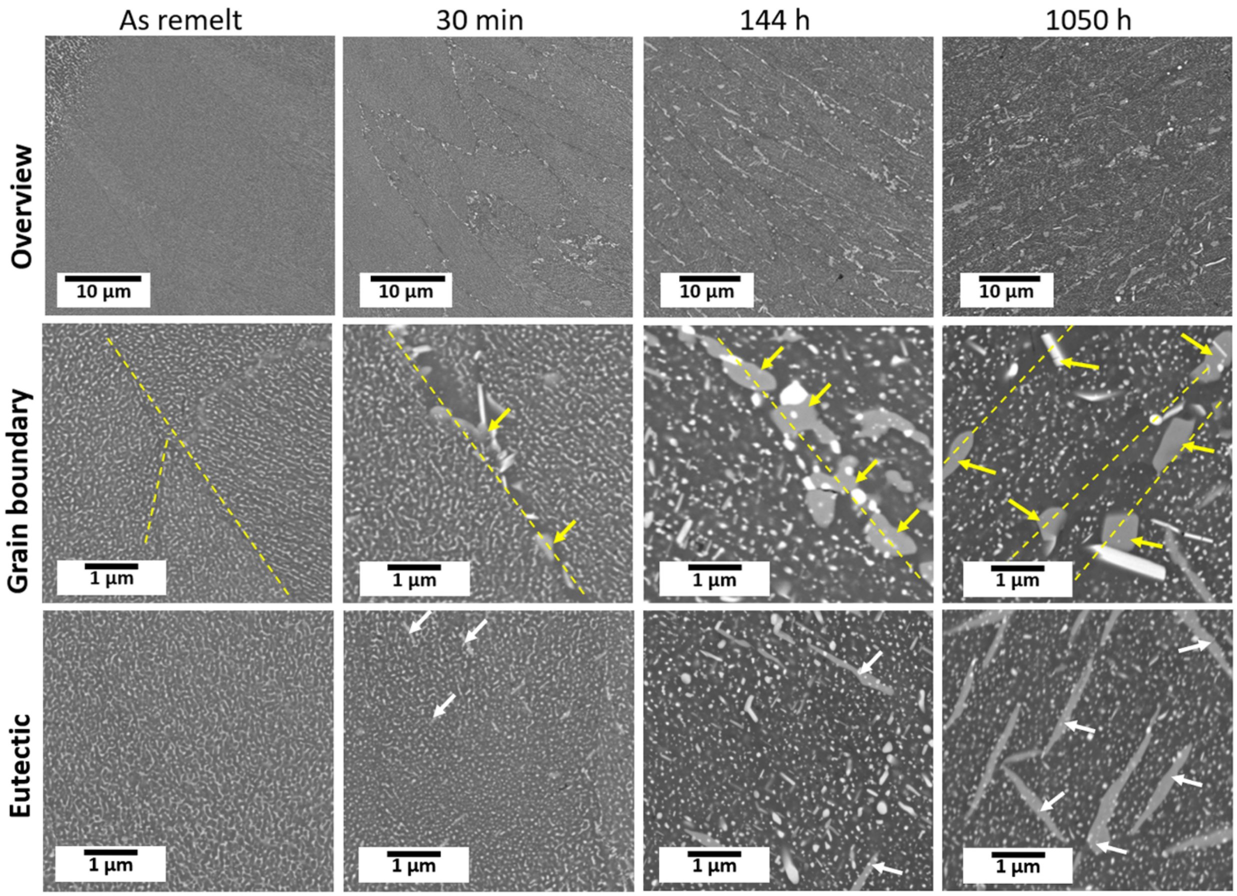

Fig. 9. Microstructure evolution during aging at 400 °C of laser-remelted Al-6Ce-3Ni-0.7Fe. (top row) overview at lower magnification; (middle row) Grain-boundaries (highlighted with yellow dash-lines), where more pronounced coarsening of precipitates (yellow arrows) creates narrow eutectic-free zones upon aging. (bottom row) Grain interior with eutectic microstructure coarsening more slowly than Ni/Fe-rich phase (grey contrast, white arrows) which appears after 30 min, and coarsens into 1-2 μm long platelets after 1050 h.

Discussion

i. Ambient-temperature strength

At ambient temperature, load transfer and Orowan strengthening are active as the dominant strengthening mechanisms in many cast eutectic systems [8,9,27,40], with both intermetallic volume fraction and inter-precipitate spacing affecting the strength of the alloy. Figure 10 shows the microhardness evolution at 400 °C for several existing similar alloys, and Table 2 summaries the microstructural features of the present Al-6Ce-3Ni-0.7Fe alloy, as well as near-eutectic Al-12.5Ce [8] and Al-10Ce-5Ni [27].

For our Al-6Ce-3Ni-0.7Fe alloy, the as-cast microhardness (566±32 MPa) is an average taken from top (563±41 MPa) and bottom (569±22 MPa) of the ingot where coarse (Fig. 2. a, c, e) and fine microstructures (Fig. 2. b, d, f) dominate, respectively. Despite the very visible difference between coarse and fine microstructures, similar average microhardness is measured, and the high standard deviation in microhardness is due to local microstructure variations with very different eutectic spacing ranging from ~200 to ~700 nm. Al-6Ce-3Ni-0.7Fe is highly hypoeutectic, with ~65 vol.% primary Al dendrites, resulting in comparable microhardness as hypoeutectic Al-7.5Ce-3.75Ni (~60 vol.% of primary Al) [27]. Binary near-eutectic Al-12.5Ce, even with near-eutectic microstructure, has a lower as-cast microhardness of ~400 MPa due to a lower volume fraction of $Al_{11}Ce_3$ phase (~14 vol.%) for load transfer and a larger eutectic lamellar spacing (~1.5 µm)[8]. Ternary Al-10Ce-5Ni has the highest as-cast microhardness (~800 MPa) with ~21 vol.% of $Al_{11}Ce_3$+Al_3Ni intermetallic phases and much finer fibers (spacing ~70-180 nm), despite a hypoeutectic microstructure with fine primary Al dendrites (~33 vol.%) [27]. Compared to this Al-10Ce-5Ni alloy, our Al-6Ce-3Ni-0.7Fe alloy has a higher fraction of coarse Al dendrites and larger eutectic phase spacing, resulting in much lower microhardness, despite having similar volume fraction of strengthening phases (~18 vol.%).

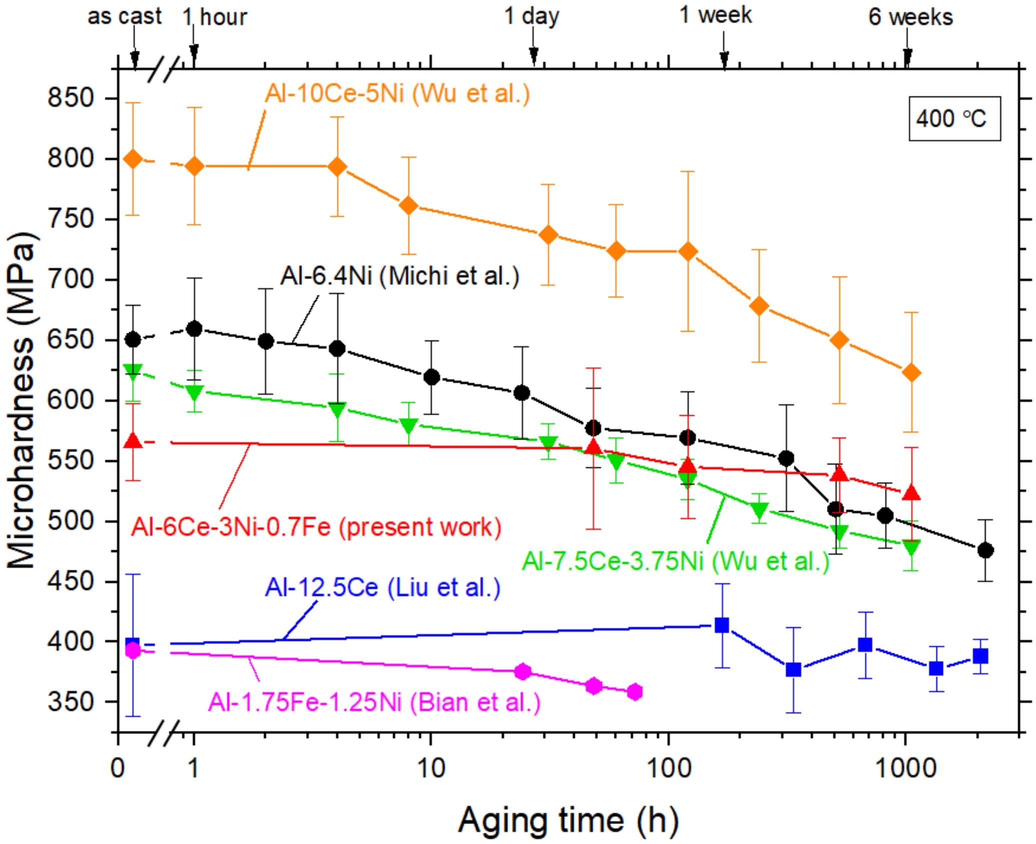

Fig.10. Evolution of Vickers microhardness during aging at 400 °C of cast Al-6Ce-3Ni-0.7Fe (red triangles, present work). For comparison, data for other cast, near-eutectic alloys are plotted: Al-6.4Ni [9], Al-12.5Ce [8], Al-10Ce-5Ni and Al-7.5Ce-3.75Ni [27], and Al-1.75Fe-1.25Ni from Ref. [35].

Table. 2. Volume fraction of intermetallic and primary Al, eutectic spacing, and eutectic morphology of Al-6Ce-3Ni-0.7Fe alloy studied here, compared to Al-12.5Ce [8] and Al-10Ce-

5Ni [27], as measured from micrographs. Intermetallic volume fraction includes, if any, primary intermetallic phases.

Alloy	Intermetallic volume fraction* (%)	Primary Al volume fraction (%)	Eutectic spacing (nm)	Eutectic morphology
Al-6Ce-3Ni-0.7Fe	~18	~65	~200-700	"Chinese script"
Al-12.5Ce [8]	~14	~0	~1500	"Chinese script"
Al-10Ce-5Ni [27]	~21	~33	~70-180	fibrous

* primary and eutectic

ii. Coarsening resistance

Ostwald ripening is controlled by volume diffusion and thus depends on both the diffusivity and solubility of individual elements in the matrix [41]. Though all alloys in Fig. 10 show good coarsening resistance, there are some noticeable differences between them due to different strengthening phases and initial microstructures (precipitate size and inter-precipitate spacing), which result from different diffusion rates and coarsening mechanisms.

Al-6Ce-3Ni-0.7Fe has excellent coarsening resistance given that both microhardness (Fig. 10) and microstructure (Fig. 4) barely decrease after long-term aging at 400 °C. Three effects can justify this observation: (i) the low solubility of Ce, Ni, and Fe at 400 ºC in the Al matrix; (ii) the low diffusivity of these elements in the Al matrix; and (iii) the coarse microstructure with relatively large eutectic spacing (>200 nm) increasing the diffusion distance needed for coarsening. Similar justifications can be applied to Al-12.5Ce [8] which shows a coarsening resistance comparable to our Al-6Ce-3Ni-0.7Fe alloy. By contrast, Al-10Ce-5Ni coarsens faster, showing spheroidized, coarse precipitates [27], and results in a large drop in microhardness (Fig. 10). This enhanced coarsening is most likely due to the fine fiber morphology (prone to pinch-off due to Rayleigh instability [42,43]), the small eutectic spacing (<200 nm), and the faster-coarsening Al_3Ni phase [27].

The strengthening phases in Al-Ce-Ni-(Fe) based alloys includes $Al_{11}Ce_3$, $Al_9(Fe,Ni)_2$, and Al_3Ni, which are all proven to have good coarsening resistance [8,9,35]. However, the relative coarsening resistance between these three phases can be examined using element's diffusivity and solubility, coarsen microstructures, and microhardness evolution. Among all alloying elements (Ce, Ni, and Fe), Ce has lowest diffusivity (4.6×10^{-19} m^2/s at 400 °C) and solubility (~0.01 at.%) in Al [25,30]. By contrast, Fe has slightly lower solubility (~0.02 at.%) and diffusivity (1.3×10^{-17} m^2/s at 400°C) in Al than Ni (~0.06 at.% and 2.3×10^{-17} m^2/s at 400°C respectively) [30,31,44]. Therefore, the Al_3Ni phase is less coarsening resistant, consistent with the observed coarsened microstructure of Al-6Ce-3Ni-0.7Fe (Fig. 4 (b)): Al_3Ni coarsens into large precipitates and partially engulfs the two other phases, $Al_{11}Ce_3$ and $Al_9(Fe,Ni)_2$, which themselves barely coarsen after aging at 400 °C for 1050 h. Comparing the microhardness evolution (Fig. 10) of near-eutectic Al-6.4Ni and Al-1.75Fe-1.25Ni, which both form fiber eutectic phases (Al_3Ni and $Al_9(Fe,Ni)_2$ respectively) with comparable spacing (~100 and ~300 nm respectively), it is apparent that Al-6.4Ni suffers from a faster microhardness drop, indicating that the Al_3Ni phase coarsens faster than the $Al_9(Fe,Ni)_2$

phase. Despite a ~100-fold difference in diffusivity between Ce and Fe in Al, $Al_{11}Ce_3$ and $Al_9(Fe,Ni)_2$ barely coarsen after aging (Fig. 4) and appear to have similar coarsening resistance.

For the extreme case of coarsening at 590 ºC (as shown in Fig. 5), $Al_{11}Ce_3$ coarsens into irregular-shaped precipitates and $Al_9(Fe,Ni)_2$ coarsens into plate-like precipitates. Unlike overaged Al-10Ce-5Ni with equiaxed, faceted $Al_{11}Ce_3$+Al_3Ni precipitates [27], the coarsened $Al_{11}Ce_3$ and $Al_9(Fe,Ni)_2$ phases show unfaceted, curved surfaces. The initial eutectic morphology and size may lead to different coarsening mechanisms. In both Al-Ni and Al-1.75Fe-1.25Ni, fibers undergo 2-dimensional coarsening (dissolution of fibers), pinch off, and Ostwald ripening [35,45]. Similar coarsening mechanisms are observed in Al-10Ce-5Ni with slightly different morphologies (fibers and interconnected, 3-dimensional network) [27]. However, in the present Al-6Ce-3Ni-0.7Fe alloy, spheroidization is barely visible, with $Al_{11}Ce_3$ and $Al_9(Fe,Ni)_2$ phases becoming larger in size and lower in number density with more rounded edges instead of facets.

iii. Creep resistance

Figures 11(a, b) compares the creep response at 300 and 350 °C of the current quaternary Al-6Ce-3Ni-0.7Fe alloy with those of binary Al-12.5Ce [8] and ternary Al-10Ce-5Ni [27]. Replicate tests were performed for each of the three alloys (except for Al-6Ce-3Ni-0.7Fe at 350 °C), revealing an offset between creep curves, especially for Al-10Ce-5Ni-a, b at 300 °C which is most likely due to microstructural differences. In both Al-6Ce-3Ni-0.7Fe and Al-10Ce-5Ni, the microstructures are inhomogeneous, with a consistent trend across the ingot: finer eutectic toward bottom with higher cooling rate. In fact, the creep resistance difference between Al-10Ce-5Ni-a (top) and -b (bottom) was indeed assigned to a variation in eutectic fibers spacing [27]. For our alloy, the offset between Al-6Ce-3Ni-0.7Fe-a (top) and -b (bottom) is less pronounced, consistent with the small difference in as-cast microhardness. The -b (bottom) alloy, with a majority of fine microstructure, shows slightly higher creep resistance likely due to smaller average eutectic spacing. A similar offset in binary Al-12.5Ce was also explained by microstructural variation due to different cooling rates within the ingot [8].

At 300 °C (Fig. 11(a)), Al-10Ce-5Ni is the most creep resistant of the three alloys because of its extremely fine eutectic fibers impeding dislocation motion. In addition, the high volume fraction of intermetallic phases and its high directionality (fibers) and high orientation with respect to the loading direction improve load transfer as compared to the Chinese script eutectic phase in Al-12.5Ce and Al-6Ce-3Ni-0.7Fe [46]. For Al-12.5Ce, load transfer and Orowan strengthening were identified as strengthening mechanisms under creep conditions, with dislocation climb made difficult by the partially interconnected Chinese script $Al_{11}Ce_3$ phase [8]. However, this binary alloy is the least creep resistant, due to a relatively coarse size and lower volume fraction of the reinforcing $Al_{11}Ce_3$ phase. On the other hand, the present quaternary Al-6Ce-3Ni-0.7Fe alloy has a slightly higher volume fraction of intermetallic, but with coarser eutectic phases and a larger fraction of soft, primary Al dendrites; the latter feature is probably crucial in reducing the creep resistance of Al-6Ce-3Ni-0.7Fe to nearly the same level as binary Al-12.5Ce. At 350 °C (Fig. 11(b)), creep resistance is reduced for all alloys as temperature increases, as expected since diffusion becomes faster, and the relative creep resistance between the three alloys shows the same trend.

The origin of the threshold stress in Al-6.4Ni [9] and Al-1.75Fe-1.25Ce [47] alloys was assigned to interactions between dislocation and precipitates, with dislocation detachment from $Al_9(Fe,Ni)_2$ fibers reported in the latter alloy. In the present study, dislocations in Al-6Ce-3Ni-0.7Fe may bypass both $Al_{11}Ce_3$ and $Al_9(Fe,Ni)_2$ phases *via* detachment and/or climb, and the coarse and interconnected nature of the eutectic phase may also inhibit dislocation climb bypass. Load transfer and Orowan strengthening, as discussed in Section 4.1, are expected to be active at both ambient and elevated temperature, justifying the observation that Al-10Ce-5Ni is stronger than Al-12.5Ce and Al-6Ce-3Ni-0.7Ni, both in terms of as-cast microhardness and creep resistance.

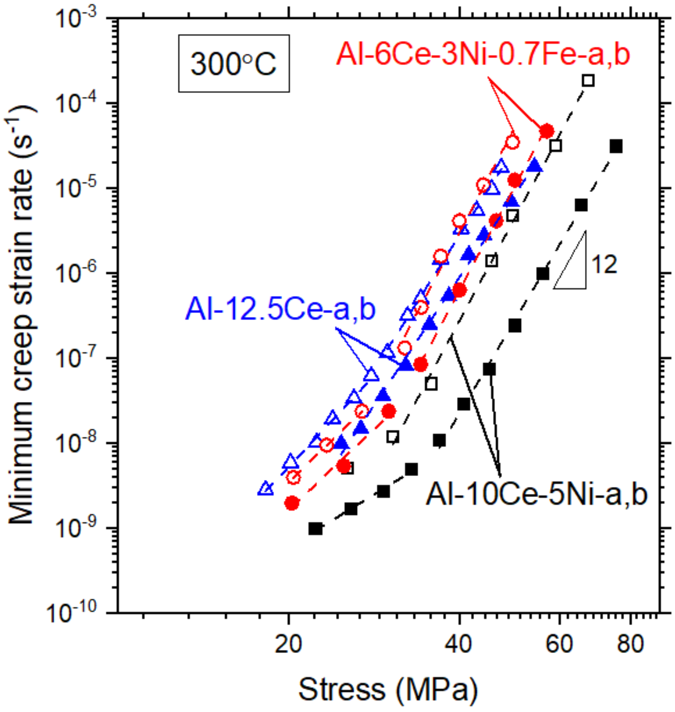

Fig. 11. Double-logarithmic plot of minimum creep strain rate vs. compressive stress, with best-fit lines drawn using Eq. (1), comparing as-cast Al-6Ce-3Ni-0.7Fe alloy (present work) to as-cast binary eutectic Al-12.5Ce (Ref. [8]) and as-cast ternary Al-10Ce-5Ni (Ref. [27]) at 300 ˚C.

iv. Laser remelting

An experimentally simulated LPBF microstructure can be achieved in cast alloys via laser-remelting of surfaces, with solidification rates similar to those achieved with powder beds. For example, a recent study [48] of laser remelted, cast Al-12Ce eutectic, under conditions similar to those prevailing in directed energy deposition, achieved a microstructure with neither cracking nor porosity, and with a refined eutectic phases thermally stable at 300 °C. In Al-8Ce-0.2Sc-0.1Zr experiments [40], laser-remelting suppressed the formation of primary intermetallic phases, with much finer eutectic phases and spacing, resulting in a doubling in microhardness as compared to the cast alloy, even after aging for 1000 h at 325 °C. In general, high solidification rates result in a refined microstructure, leading to superior hardness (and thus strength), as compared to the cast alloy of the same composition.

In the present study, laser-remelted Al-6Ce-3Ni-0.7Fe shows a fully refined eutectic microstructure with a eutectic spacing ~50-70 nm (Fig. 8), replacing the coarser, hypoeutectic structure in the as-cast counterpart (eutectic spacing ~200-700 nm). The high undercooling achieved via laser-remelting suppresses the formation of primary Al dendrites [49] and forms a continuous network of eutectic phases varying slightly in spacing due to the thermal gradient variation toward the center of the melt-pool: somewhat coarser (resp. finer) eutectic (Fig. 8 c/d) is formed at lower (resp. higher) solidification rate away from (resp. closer to) the melt pool boundaries. The fully eutectic microstructure, despite the hypoeutectic composition of alloy, can be explained by the high undercooling and the non-faceted/faceted $Al/Al_{11}Ce_3$ interface which leads to skewed coupled growth towards the Ce-rich composition, as found in eutectic systems with one phase having anisotropic growth characteristics [50–52]. Within the coupled zone, the coupled eutectic grows faster than the primary phases, so that fully eutectic solidification is achieved with a range of compositions and undercoolings. For example, hypereutectic Al-15Ce forms a fully eutectic microstructure via arc surface rapid melting [52], and hypoeutectic Al-10Ce powders result in a near-eutectic microstructure after LPBF [24].

Refinement of the microstructure, in addition to the fully eutectic microstructure without weak Al dendrites, *via* rapid solidification leads to a doubling in microhardness, from ~600 MPa (cast) to ~1200 MPa (laser-remelted). However, the microhardness of the laser-remelted alloy decreases steadily upon aging at 400 ºC, eventually reaching ~800 MPa after 1050 h aging, as shown in Fig. 3. Figure 9 shows the evolution of the remelted microstructure upon aging at 400 ºC. First, in the as-remelted state, a homogeneous, very fine eutectic microstructure exists in the melt-pool and at melt pool boundaries. After short-time aging (30 min), precipitates slightly coarsen at grain boundaries, while the eutectic phases pinch off, and needle-like Ni/Fe-rich phase (grey contrast) forms and coarsens. After 144 h aging, accelerated coarsening is visible along grain boundaries, and, within the grain, spheroidized eutectic and Ni/Fe-rich phases continue to coarsen. Finally, after long-term aging (1050 h, 6 weeks), coarser precipitates create visible eutectic-free zones along grain boundaries and the Ni/Fe-rich needles grow to lengths of 1-2 μm, with an orientation relationship with respect to each grain. Thus, at 400 ºC, the fine rapidly solidified microstructures coarsens steadily, together with a drop in microhardness (Fig. 3), as expected from an extremely fine interlamellar eutectic spacing enabling mass transfer by diffusion, together with pinching off (followed by enhanced coarsening rate [45]) to reduce surface area. In addition, non-equilibrium solidification may induce formation of metastable phases and therefore phase transformation upon aging [53]. The definitive identification of the Ni/Fe-rich phase formed within grains during aging (as highlighted by white arrows in Fig.9) is beyond the scope of this study, and it could possibly result from coarsening, phase transformation, or precipitation from highly supersaturated solid solution (matrix).

From the laser-remelting results, it is likely that LPBF of Al-6Ce-3Ni-0.7Fe powders will achieve similar initial microstructure and microhardness, and similar evolution upon aging. Hardness measurements of the surface remelted cast alloy (Fig. 3) indicate that bulk mechanical testing (e.g., tensile and creep testing) of as-fabricated AM specimens should show significantly enhanced strength from the extremely fine eutectics and the absence of soft Al dendrites, as compared to cast sample; however, the coarsening of the microstructure must be taken into account for long-term exposure at 400 ºC.

Conclusions

The microstructure, thermal stability, ambient and elevated temperature strengthening of cast, hypoeutectic Al-6Ce-3Ni-0.7Fe (wt%) were studied, leading to the following conclusions:

1. A range of fine and coarse microstructures is found in as-cast Al-6Ce-3Ni-0.7Fe, likely due to variation in cooling rates, where volume fraction of fine/coarse microstructure increase/decrease from top to bottom of the ingot.
    a) The finer microstructure consists of fine Al dendrites and interdendritic binary Al-$Al_{11}Ce_3$ eutectic containing micron-sized $Al_9(Fe,Ni)_2$ plates.
    b) The coarser microstructure consists of long Al dendrites containing $Al_9(Fe,Ni)_2$ plates, with interdendritic regions displaying alternating Al-$Al_{11}Ce$/Al-$Al_9(Fe,Ni)_2$ binary eutectics.
2. During aging at 400°C, good coarsening resistance is observed, with only a small decrease in microhardness after 1050 h. The cast microstructure remains mostly unchanged, except for infrequent occurrences of coarsened Al_3Ni particles which partially engulfed finer $Al_{11}Ce_3$ and $Al_9(Fe,Ni)_2$ particles. Among these three intermetallic phases, Al_3Ni is the least coarsening-resistant, while $Al_{11}Ce_3$ and $Al_9(Fe,Ni)_2$ have comparable low coarsening resistance.
3. During overaging at 590 °C for 24 h, $Al_{11}Ce_3$ and $Al_9(Fe,Ni)_2$ eutectics became coarse, irregular-shaped precipitates without faceting, but the decrease in hardness remains relatively mild (16%).
4. With high fraction of intermetallic (~18 vol.%) and coarse Al dendrites (~65 vol.%) and large eutectic phase spacing (~200-700 nm), Al-6Ce-3Ni-0.7Fe has as-cast microhardness of 566±32 MPa, which is higher than that of binary Al-12.5Ce yet lower than ternary Al-10Ce-5Ni (both with higher Ce content).
5. Despite its high volume fraction of intermetallic phases, Al-6Ce-3Ni-0.7Fe, with its weak Al dendrites and relatively coarse eutectic spacing, shows a creep resistance similar to that of binary Al-12.5Ce.
6. Laser-remelted Al-6Ce-3Ni-0.7Fe shows a fully eutectic microstructure, achieved *via* high undercooling from rapid solidification of the hypoeutectic composition. The spacing of the eutectic network varies slightly across the melt pool due to thermal gradients. The highly refined eutectic microstructure without Al dendrites doubles the as-cast microhardness but undergoes coarsening during long-term aging at 400°C, because of reduced diffusion

distances; nevertheless, microhardness is ~30% higher compared to the as-cast alloy after 1050 h of aging.

Data availability - All data included in this study are available upon request from the corresponding author.

Acknowledgments - TW was supported by the GO! Program from Oak Ridge National Laboratory (ORNL). This research was co-sponsored by the U.S. Department of Energy, Office of Energy Efficiency and Renewable Energy, Advanced Manufacturing Office and Vehicle Technologies Office Propulsion Materials Program (AP and AS). This work made use of the Materials Characterization and Imaging Facility and EPIC facility of Northwestern University's NUANCE Center, which both receive support from the MRSEC Program (NSF DMR-1720139) of the Materials Research Center at Northwestern University. X-ray diffraction was conducted by Dr. C.M. Fancher (ORNL) as part of a user project at the Center for Nanophase Materials Sciences (CNMS), which is a US Department of Energy, Office of Science User Facility at ORNL. Mr. F.M. Carter (Northwestern University) is gratefully acknowledged for experimental support with the laser-remelting trials, which were performed at the CHiMad Metals Processing Facility at Northwestern University (CHiMad is supported by the U.S. Department of Commerce, National Institute of Standards and Technology, under award 70NANB14H012).

CRediT authorship contribution statement - Tiffany Wu: Methodology, Investigation, Data curation, Formal analysis, Visualization, Writing - original draft, Writing – review & editing. Alex Plotkowski – Methodology, Conceptualization, Funding acquisition, Supervision, Writing – review & editing. Amit Shyam – Methodology, Conceptualization, Funding acquisition, Supervision, Writing – review & editing. David C. Dunand: Methodology, Conceptualization, Funding acquisition, Supervision, Writing - review & editing.

Declaration of Competing Interests - DCD discloses a financial interest in NanoAl (part of Aluminum Dynamics Inc.) which is active in the field of cast and additively-manufactured aluminum alloys.

Supplementary Information

Fig. S1.X-ray diffraction patterns for as-cast Al-6Ce-3Ni-0.7Fe alloy, comparing between (a) top and bottom of the ingot, and (b) as-cast (from top of the ingot) and overaged (590°C, 24h) samples. No new phase is observed after overaging.

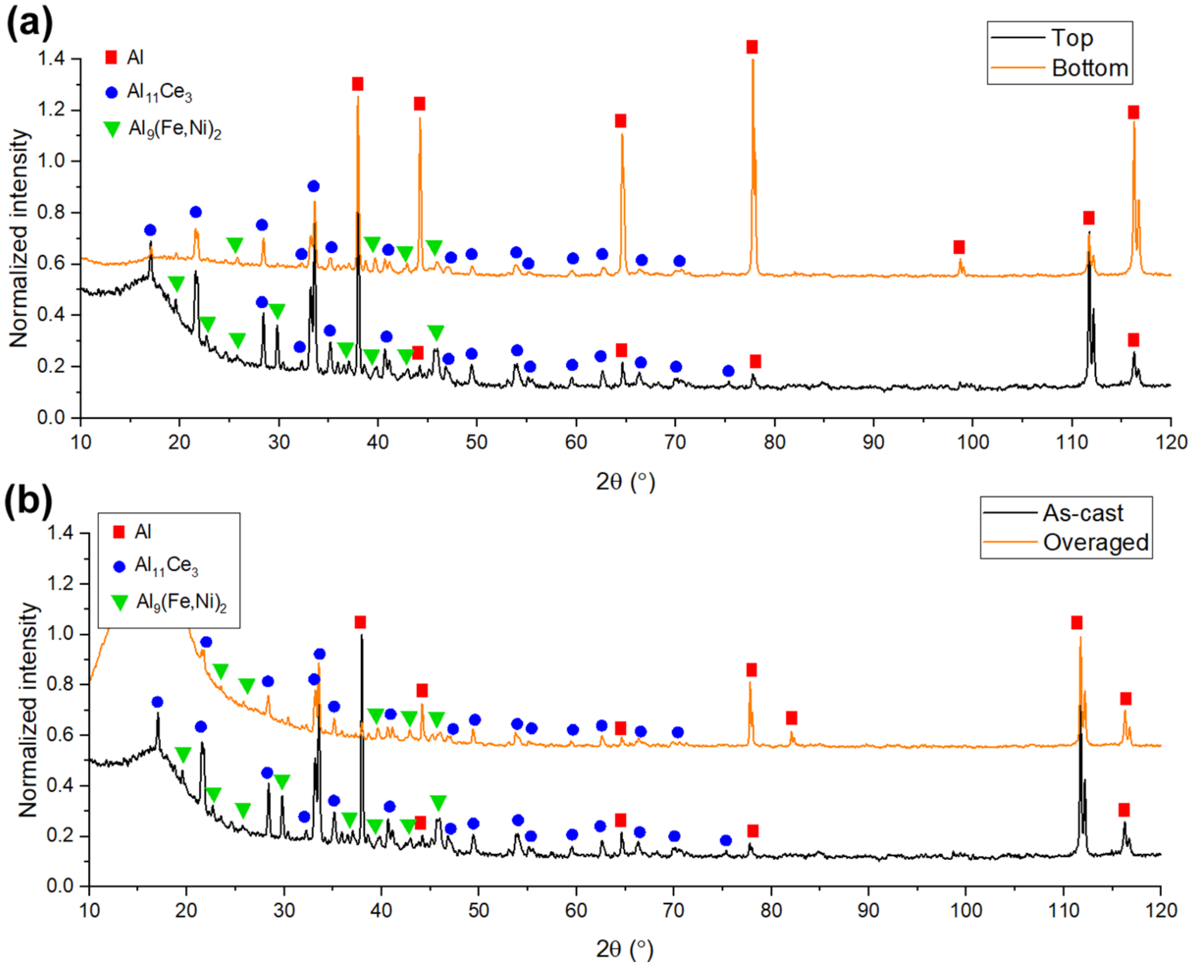

Fig. S2. BSE-SEM micrograph of as-cast Al-6Ce-3Ni-0.7Fe, showing primary Al dendrites and a rare case of interdendritic ternary eutectic. The yellow box insert shows high magnification of coupled growth of ternary eutectic identified as Al (black) + $Al_9(Fe,Ni)_2$ (grey) + $Al_{11}Ce_3$ (white).

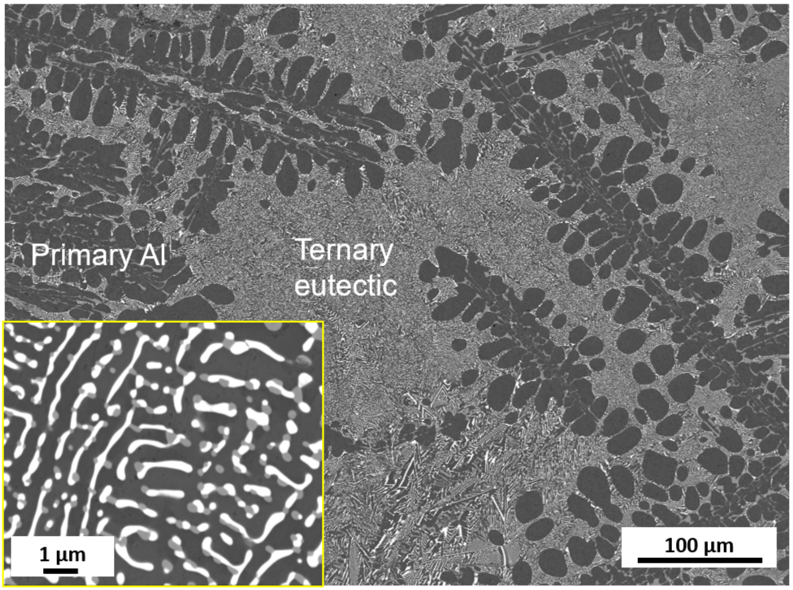

Fig. S3. BSE-SEM micrograph of as-cast Al-6Ce-3Ni-0.7Fe, in one of the rare regions where Al_3Ni is present, with corresponding EDS maps, showing phases at different contrast (from darkest to brightest): Al-matrix, $Al_9(Fe,Ni)_2$, Al_3Ni (eutectic-like), and $Al_{11}Ce_3$.

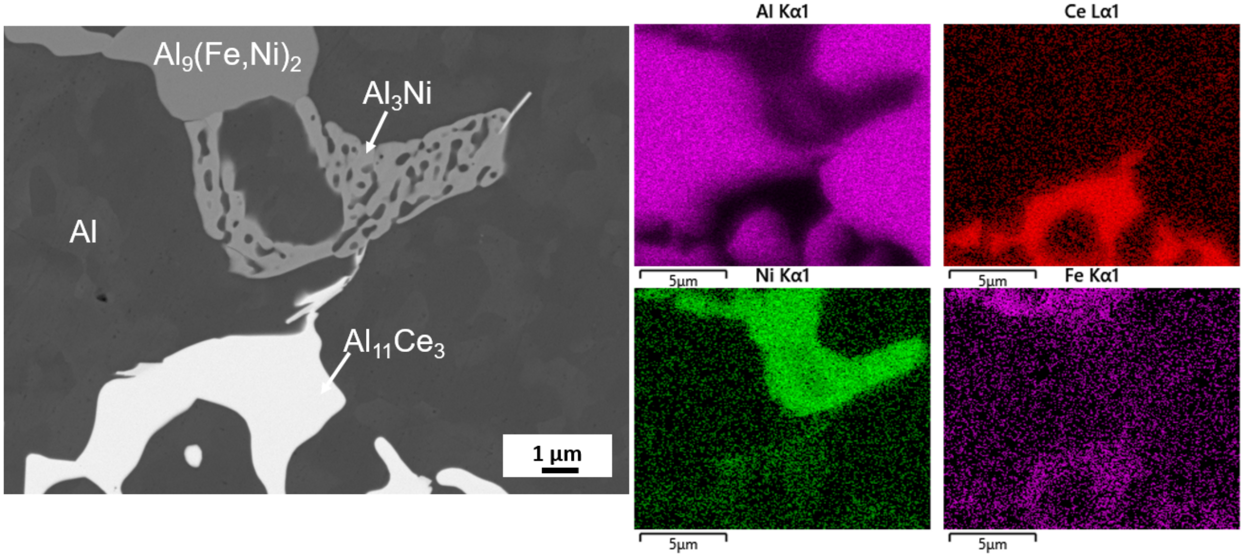

References

[1] C. Sigli, F. De Geuser, A. Deschamps, J. Lépinoux, M. Perez, Recent advances in the metallurgy of aluminum alloys. Part II: Age hardening, Comptes Rendus Physique. 19 (2018) 688–709. https://doi.org/10.1016/j.crhy.2018.10.012.

[2] K.E. Knipling, D.N. Seidman, D.C. Dunand, Ambient- and high-temperature mechanical properties of isochronally aged Al–0.06Sc, Al–0.06Zr and Al–0.06Sc–0.06Zr (at.%) alloys, Acta Materialia. 59 (2011) 943–954. https://doi.org/10.1016/j.actamat.2010.10.017.

[3] C. Booth-Morrison, D.C. Dunand, D.N. Seidman, Coarsening resistance at 400°C of precipitation-strengthened Al–Zr–Sc–Er alloys, Acta Materialia. 59 (2011) 7029–7042. https://doi.org/10.1016/j.actamat.2011.07.057.

[4] Y. Sun, Q. Pan, Y. Luo, S. Liu, W. Wang, J. Ye, Y. Shi, Z. Huang, S. Xiang, Y. Liu, The effects of scandium heterogeneous distribution on the precipitation behavior of Al3(Sc, Zr) in aluminum alloys, Materials Characterization. 174 (2021) 110971. https://doi.org/10.1016/j.matchar.2021.110971.

[5] K.E. Knipling, D.C. Dunand, D.N. Seidman, Criteria for developing castable, creep-resistant aluminum-based alloys – A review, MEKU. 97 (2006) 246–265. https://doi.org/10.3139/146.101249.

[6] R. Li, H. Chen, H. Zhu, M. Wang, C. Chen, T. Yuan, Effect of aging treatment on the microstructure and mechanical properties of Al-3.02Mg-0.2Sc-0.1Zr alloy printed by selective laser melting, Materials & Design. 168 (2019) 107668. https://doi.org/10.1016/j.matdes.2019.107668.

[7] W. Kang, H.Y. Li, S.X. Zhao, Y. Han, C.L. Yang, G. Ma, Effects of homogenization treatments on the microstructure evolution, microhardness and electrical conductivity of dilute Al-Sc-Zr-Er alloys, Journal of Alloys and Compounds. 704 (2017) 683–692. https://doi.org/10.1016/j.jallcom.2017.02.043.

[8] Y. Liu, R.A. Michi, D.C. Dunand, Cast near-eutectic Al-12.5 wt.% Ce alloy with high coarsening and creep resistance, Materials Science and Engineering: A. 767 (2019) 138440. https://doi.org/10.1016/j.msea.2019.138440.

[9] R.A. Michi, J.P. Toinin, D.N. Seidman, D.C. Dunand, Ambient- and elevated-temperature strengthening by Al3Zr-Nanoprecipitates and Al3Ni-Microfibers in a cast Al-2.9Ni-0.11Zr-0.02Si-0.005Er (at.%) alloy, Materials Science and Engineering: A. 759 (2019) 78–89. https://doi.org/10.1016/j.msea.2019.05.018.

[10] A. Shyam, S. Roy, D. Shin, J.D. Poplawsky, L.F. Allard, Y. Yamamoto, J.R. Morris, B. Mazumder, J.C. Idrobo, A. Rodriguez, T.R. Watkins, J.A. Haynes, Elevated temperature microstructural stability in cast AlCuMnZr alloys through solute segregation, Materials Science and Engineering: A. 765 (2019) 138279. https://doi.org/10.1016/j.msea.2019.138279.

[11] J.U. Rakhmonov, S. Bahl, A. Shyam, D.C. Dunand, Cavitation-resistant intergranular precipitates enhance creep performance of θ′-strengthened Al-Cu based alloys, Acta Materialia. 228 (2022) 117788. https://doi.org/10.1016/j.actamat.2022.117788.

[12] J.D. Poplawsky, B.K. Milligan, L.F. Allard, D. Shin, P. Shower, M.F. Chisholm, A. Shyam, The synergistic role of Mn and Zr/Ti in producing θ′/L12 co-precipitates in Al-Cu alloys, Acta Materialia. 194 (2020) 577–586. https://doi.org/10.1016/j.actamat.2020.05.043.

[13] F. Czerwinski, Critical Assessment 40: A search for the eutectic system of high-temperature cast aluminium alloys, Materials Science and Technology. 37 (2021) 683–692. https://doi.org/10.1080/02670836.2021.1940670.

[14] J.A. Glerum, J.-E. Mogonye, D.C. Dunand, Creep properties and microstructure evolution at 260–300 °C of AlSi10Mg manufactured via laser powder-bed fusion, Materials Science and Engineering: A. 843 (2022) 143075. https://doi.org/10.1016/j.msea.2022.143075.

[15] Q. Yan, B. Song, Y. Shi, Comparative study of performance comparison of AlSi10Mg alloy prepared by selective laser melting and casting, Journal of Materials Science & Technology. 41 (2020) 199–208. https://doi.org/10.1016/j.jmst.2019.08.049.

[16] X. Zhu, H. Yang, X. Dong, S. Ji, The effects of varying Mg and Si levels on the microstructural inhomogeneity and eutectic Mg2Si morphology in die-cast Al–Mg–Si alloys, J Mater Sci. 54 (2019) 5773–5787. https://doi.org/10.1007/s10853-018-03198-6.

[17] H.B. Smartt, L.K. Tu, T.H. Courtney, Elevated Temperature Stability of the AI-AI3Ni Eutectic Composite, Metallurgical Transactions. 2 (1971) 2717–2727. https://doi.org/10.1007/BF02814917.

[18] P. Pandey, S.K. Makineni, B. Gault, K. Chattopadhyay, On the origin of a remarkable increase in the strength and stability of an Al rich Al-Ni eutectic alloy by Zr addition, Acta Materialia. 170 (2019) 205–217. https://doi.org/10.1016/j.actamat.2019.03.025.

[19] C. Suwanpreecha, P. Pandee, U. Patakham, C. Limmaneevichitr, New generation of eutectic Al-Ni casting alloys for elevated temperature services, Materials Science and Engineering: A. 709 (2018) 46–54. https://doi.org/10.1016/j.msea.2017.10.034.

[20] F. Czerwinski, Thermal Stability of Aluminum-Nickel Binary Alloys Containing the Al-Al3Ni Eutectic, Metall Mater Trans A. 52 (2021) 4342–4356. https://doi.org/10.1007/s11661-021-06372-9.

[21] M. Yi, P. Zhang, C. Yang, P. Cheng, S. Guo, G. Liu, J. Sun, Improving creep resistance of Al-12 wt.% Ce alloy by microalloying with Sc, Scripta Materialia. 198 (2021) 113838. https://doi.org/10.1016/j.scriptamat.2021.113838.

[22] Z.C. Sims, O.R. Rios, D. Weiss, P.E.A. Turchi, A. Perron, J.R.I. Lee, T.T. Li, J.A. Hammons, M. Bagge-Hansen, T.M. Willey, K. An, Y. Chen, A.H. King, S.K. McCall, High performance aluminum–cerium alloys for high-temperature applications, Mater. Horiz. 4 (2017) 1070–1078. https://doi.org/10.1039/C7MH00391A.

[23] H. Hyer, A. Mehta, K. Graydon, N. Kljestan, M. Knezevic, D. Weiss, B. McWilliams, K. Cho, Y. Sohn, High strength aluminum-cerium alloy processed by laser powder bed fusion, Additive Manufacturing. 52 (2022) 102657. https://doi.org/10.1016/j.addma.2022.102657.

[24] L. Zhou, T. Huynh, S. Park, H. Hyer, A. Mehta, S. Song, Y. Bai, B. McWilliams, K. Cho, Y. Sohn, Laser powder bed fusion of Al–10 wt% Ce alloys: microstructure and tensile property, J Mater Sci. (2020). https://doi.org/10.1007/s10853-020-05037-z.

[25] S.P. Murarka, R.P. Agarwala, DIFFUSION OF RARE EARTH ELEMENTS IN ALUMINUM., Bhabha Atomic Research Centre, Bombay (India), 1968.

[26] D.S. Ng, D.C. Dunand, Coarsening- and Creep-Resistant Cast Hypoeutectic Al-Ce-Mg Alloy, SSRN Journal. (2019). https://doi.org/10.2139/ssrn.3485043.

[27] T. Wu, A. Plotkowski, A. Shyam, D.C. Dunand, Microstructure and creep properties of cast near-eutectic Al–Ce–Ni alloys, Materials Science and Engineering: A. 833 (2022) 142551. https://doi.org/10.1016/j.msea.2021.142551.

[28] T. Wu, D.C. Dunand, Microstructure and thermomechanical properties of Al11Ce3, Intermetallics. 148 (2022) 107636. https://doi.org/10.1016/j.intermet.2022.107636.

[29] R.A. Michi, K. Sisco, S. Bahl, Y. Yang, J.D. Poplawsky, L.F. Allard, R.R. Dehoff, A. Plotkowski, A. Shyam, A creep-resistant additively manufactured Al-Ce-Ni-Mn alloy, Acta Materialia. 227 (2022) 117699. https://doi.org/10.1016/j.actamat.2022.117699.

[30] L.F. Mondolfo, Aluminum Alloys: Structure and Properties, Butterworths, 1976.

[31] K. Hirano, R.P. Agarwala, M. Cohen, Diffusion of iron, nickel and cobalt in aluminum, Acta Metallurgica. 10 (1962) 857–863. https://doi.org/10.1016/0001-6160(62)90100-1.

[32] P. Budberg, A. Prince, G. Cacciamani, R. Ferro, B. Grushko, P. Perrot, R. Schmid-Fetzer, Materials Science International Team, MSIT®, Al-Fe-Ni Ternary Phase Diagram Evaluation, (n.d.). https://materials-springer-com.turing.library.northwestern.edu/msi/docs/sm_msi_r_10_010205_02 (accessed November 10, 2022).

[33] M. K. Premkumar, A. Lawley, M. J. Koczak, Mechanical behavior of powder metallurgy A1-Fe-Ni alloys, Materials Science and Engineering: A. 174 (1994) 127–139.

[34] F. Průša, D. Vojtěch, A. Michalcová, I. Marek, Mechanical properties and thermal stability of Al–Fe–Ni alloys prepared by centrifugal atomisation and hot extrusion, Materials Science and Engineering: A. 603 (2014) 141–149. https://doi.org/10.1016/j.msea.2014.02.081.

[35] Z. Bian, S. Dai, L. Wu, Z. Chen, M. Wang, D. Chen, H. Wang, Thermal stability of Al–Fe–Ni alloy at high temperatures, Journal of Materials Research and Technology. 8 (2019) 2538–2548. https://doi.org/10.1016/j.jmrt.2019.01.028.

[36] Z. Bian, Y. Liu, S. Dai, Z. Chen, M. Wang, D. Chen, H. Wang, Regulating microstructures and mechanical properties of Al–Fe–Ni alloys, Progress in Natural Science: Materials International. 30 (2020) 54–62. https://doi.org/10.1016/j.pnsc.2019.12.006.

[37] H. Ding, Y. Xiao, Z. Bian, Y. Wu, H. Yang, H. Wang, H. Wang, Design, microstructure and thermal stability of a novel heat-resistant Al-Fe-Ni alloy manufactured by selective laser melting, Journal of Alloys and Compounds. 885 (2021) 160949. https://doi.org/10.1016/j.jallcom.2021.160949.

[38] E. Arzt, J. Rösler, The kinetics of dislocation climb over hard particles—II. Effects of an attractive particle-dislocation interaction, Acta Metallurgica. 36 (1988) 1053–1060. https://doi.org/10.1016/0001-6160(88)90159-9.

[39] T. Wu, L.F. Allard, A. Plotkowski, A. Shyam, D.C. Dunand, Unpublished work, (n.d.).

[40] J.U. Rakhmonov, D. Weiss, D.C. Dunand, Comparing evolution of precipitates and strength upon aging of cast and laser-remelted Al–8Ce-0.2Sc-0.1Zr (wt.%), Materials Science and Engineering: A. 840 (2022) 142990. https://doi.org/10.1016/j.msea.2022.142990.

[41] H.A. Calderon, P.W. Voorhees, J.L. Murray, G. Kostorz, Ostwald ripening in concentrated alloys, Acta Metallurgica et Materialia. 42 (1994) 991–1000. https://doi.org/10.1016/0956-7151(94)90293-3.

[42] L.K. Aagesen, A.E. Johnson, J.L. Fife, P.W. Voorhees, M.J. Miksis, S.O. Poulsen, E.M. Lauridsen, F. Marone, M. Stampanoni, Universality and self-similarity in pinch-off of rods by bulk diffusion, Nature Phys. 6 (2010) 796–800. https://doi.org/10.1038/nphys1737.

[43] L.K. Aagesen, A.E. Johnson, J.L. Fife, P.W. Voorhees, M.J. Miksis, S.O. Poulsen, E.M. Lauridsen, F. Marone, M. Stampanoni, Pinch-off of rods by bulk diffusion, Acta Materialia. 59 (2011) 4922–4932. https://doi.org/10.1016/j.actamat.2011.04.036.

[44] H. Okamoto, Al-Ni (Aluminum-Nickel), J. Phase Equilib. Diffus. 25 (2004) 394. https://doi.org/10.1361/15477030420232.

[45] H.B. Smartt, T.H. Courtney, The Kineticsof Coarsening in the AI-AI3Ni System, METALLURGICAL TRANSACTIONS A. (n.d.) 4.

[46] D.V. Kolluru, T.M. Pollock, Numerical modeling of the creep behavior of unidirectional eutectic composites, Acta Materialia. 46 (1998) 2859–2876. https://doi.org/10.1016/S1359-6454(97)00454-0.

[47] Z. Bian, C. Yang, H. Zhu, D. Zhao, M. Wang, H. Zhang, Z. Chen, H. Wang, Understanding the creep property of heat-resistant Al alloy by analyzing eutectic phase/matrix interface structures, Materials Research Letters. 11 (2023) 205–212. https://doi.org/10.1080/21663831.2022.2136016.

[48] A. Plotkowski, O. Rios, N. Sridharan, Z. Sims, K. Unocic, R.T. Ott, R.R. Dehoff, S.S. Babu, Evaluation of an Al-Ce alloy for laser additive manufacturing, Acta Materialia. 126 (2017) 507–519. https://doi.org/10.1016/j.actamat.2016.12.065.

[49] B.P. Ramakrishnan, Q. Lei, A. Misra, J. Mazumder, Effect of laser surface remelting on the microstructure and properties of Al-Al2Cu-Si ternary eutectic alloy, Sci Rep. 7 (2017) 13468. https://doi.org/10.1038/s41598-017-13953-5.

[50] W. Kurz, Fisher D.J., Fundamentals of solidification, 3rd ed., Trans Tech Publications Ltd., n.d.

[51] K. Sisco, A. Plotkowski, Y. Yang, D. Leonard, B. Stump, P. Nandwana, R. Dehoff, S. Babu, Microstructure and Properties of Additively Manufactured Al-Ce-Mg Alloys, In Review, 2020. https://doi.org/10.21203/rs.3.rs-121359/v1.

[52] Y. Guo, J. Hu, Q. Han, B. Sun, J. Wang, C. Liu, Microstructure diversity dominated by the interplay between primary intermetallics and eutectics for Al-Ce heat-resistant alloys, Journal of Alloys and Compounds. 899 (2022) 162914. https://doi.org/10.1016/j.jallcom.2021.162914.

[53] J.U. Rakhmonov, D. Weiss, D.C. Dunand, Solidification microstructure, aging evolution and creep resistance of laser powder-bed fused Al-7Ce-8Mg (wt%), Additive Manufacturing. 55 (2022) 102862. https://doi.org/10.1016/j.addma.2022.102862.